Wintertime Rossby Wave Breaking Persistence in Extended-Range Seasonal Forecasts of Atlantic Tropical Cyclone Activity

JHORDANNE J. JONES,[a] MICHAEL M. BELL,[a] PHILIP J. KLOTZBACH,[a] AND ELIZABETH A. BARNES[a]

[a] *Department of Atmospheric Science, Colorado State University, Fort Collins, Colorado*

(Manuscript received 16 March 2021, in final form 12 December 2021)

ABSTRACT: In this study, we examine the wintertime environmental precursors of summer anticyclonic wave breaking (AWB) over the North Atlantic region and assess the applicability of these precursors in predicting AWB impacts on seasonal tropical cyclone (TC) activity. We show that predictors representing the environmental impacts of subtropical AWB on seasonal TC activity improve the skill of extended-range seasonal forecasts of TC activity. There is a significant correlation between boreal winter and boreal summer AWB activity via AWB-forced phases of the quasi-stationary North Atlantic Oscillation (NAO). Years with above-normal boreal summer AWB activity over the North Atlantic region also show above-normal AWB activity in the preceding boreal winter that tends to force a positive phase of the NAO that persists through the spring. These conditions are sustained by continued AWB throughout the year, particularly when El Niño–Southern Oscillation plays less of a role at forcing the large-scale circulation. While individual AWB events are synoptic and nonlinear with little predictability beyond 8–10 days, the strong dynamical connection between winter and summer wave breaking lends enough persistence to AWB activity to enable predictability of its potential impacts on TC activity. We find that the winter–summer relationship improves the skill of extended-range seasonal forecasts from as early as an April lead time, particularly for years when wave breaking has played a crucial role in suppressing TC development.

KEYWORDS: Hurricanes; Wave breaking; North Atlantic Oscillation; Tropical cyclones; Statistical forecasting; Seasonal variability

1. Introduction

North Atlantic (hereafter simply Atlantic) seasonal tropical cyclone (TC) prediction is complex due to the overlapping driving forces of several large-scale climate phenomena. The main large-scale drivers of the Atlantic atmospheric circulation include the Atlantic meridional mode (AMM; Kossin and Vimont 2007; Patricola et al. 2014) and El Niño–Southern Oscillation (ENSO; Gray 1984; Camargo et al. 2007) on interannual time scales and the Atlantic multidecadal oscillation (AMO; Goldenberg et al. 2001; Klotzbach and Gray 2008) on multidecadal time scales. Through their influence on the large-scale atmospheric circulation, these oscillations provide substantial predictability of the tropical environment, accounting for more than 30% of the explained variance (Chelliah and Bell 2004; Aiyyer and Thorncroft 2006; Jones et al. 2020). Consequently, environmental metrics closely related to ENSO and the AMM are frequently used as predictors for seasonal TC activity (Klotzbach and Gray 2008; Klotzbach et al. 2017). However, these drivers are at times insufficient to account for certain changes that occur from month to month that may be attributed to intraseasonal variability.

Recently, several studies have identified a strong relationship between seasonal TC activity and boreal summer (hereafter summer) subtropical anticyclonic Rossby wave breaking (Zhang et al. 2016, 2017; Jones et al. 2020; Papin et al. 2020). Anticyclonic Rossby wave breaking (AWB) is the irreversible overturning of potential vorticity (PV) contours against a strong PV gradient that results in the vertical mixing of dry midlatitude high-PV air into lower latitudes (McIntyre and Palmer 1983). The reverse dynamical effect can be observed with cyclonic wave breaking where moister low-PV air is mixed into the midlatitude atmosphere. Synoptic-scale AWB episodes on the 350-K isentropic surface occur frequently over the subtropical Atlantic (Zhang et al. 2017; Papin et al. 2020), peaking between July and September (Fig. 1). Further description of how AWB is detected and quantified is given in section 2. Anomalously intense AWB is associated with increased vertical wind shear (VWS) and decreased moisture content over the tropical Atlantic, conditions that typically suppress the development of TCs (Jones et al. 2020). Anomalous westerly VWS is generally introduced to the tropical environment via the downstream edge of equatorward PV streamers.

The 2013 Atlantic hurricane season was characterized by high tropical Atlantic sea surface temperatures (SSTs), sustained cool neutral ENSO conditions, and anomalously low sea level pressure over the Caribbean basin (Klotzbach and Gray 2013; Saunders et al. 2020), conditions that suggested a favorable environment for enhanced TC activity. However, Klotzbach and Gray (2013) also observed that the August–October 2013 environment was characterized by strong upper-level convergence indicating subsidence and reduced rainfall over the Atlantic. Zhang et al. (2016) later showed that the 2013 season was suppressed through anomalously frequent subtropical AWB in August due to a stronger and more eastward-shifted Atlantic midlatitude jet. Anomalous AWB continued into September, consequently reducing moisture and relative humidity over the Atlantic main development region (MDR), generally defined as 10°–20°N, 85°–20°W. These observations suggest that metrics of subseasonal AWB

Corresponding author: Jhordanne Jones, jhordanne.jones@colostate.edu

DOI: 10.1175/JCLI-D-21-0213.1

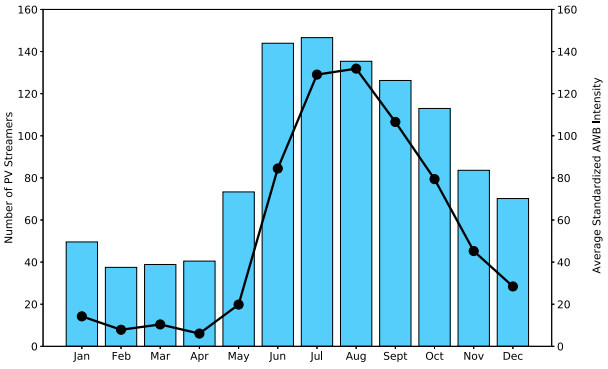

FIG. 1. Average standardized monthly anticyclonic wave breaking intensity (AWB; black solid line) and number of equatorward potential vorticity (PV) streamers (blue bars) over the Atlantic from 1979 to 2019. The standardized average AWB intensity or the potential vorticity streamer intensity (PVSI) is defined as the standardized PV anomaly integrated over the areal extent of each PV streamer (Papin et al. 2020). Details on PV streamer detection are outlined in section 2c.

impacts could support current prediction schemes to account for years in which subtropical Atlantic dynamics drive the tropical environment.

The intrinsic predictability of weather states and extremes based on certain large-scale atmospheric phenomena is often intermittent and inconsistent over time (Mariotti et al. 2020), depending on the forecast window. Klotzbach and Gray (2004) observed a degradation in the African rainfall relationship with Atlantic TCs, while Camargo and Sobel (2010) noted that the quasi-biennial oscillation (QBO)–Atlantic TC relationship was no longer significant. Both predictors had a strong relationship with seasonal TC activity in the Atlantic from the 1950s to the mid-1990s but have shown little skill in recent years. A similar situation exists with AWB variability. Subtropical Atlantic AWB dynamics are synoptic and nonlinear in nature (Abatzoglou and Magnusdottir 2006b; Bach et al. 2019), and their predictability depends in large part on the background state, the dominant subseasonal or seasonal atmospheric influence—for example, subseasonal influences of the Madden–Julian oscillation (MJO; Madden and Julian 1972)—and consequent evolution of the environment via eddy fluxes. AWB activity shows significant negative correlations with TC activity on both subseasonal and seasonal time scales, but the strength of the AWB–TC relationship may vary from year to year (Li et al. 2018; Zhang and Wang 2019).

The scientific literature currently provides little guidance for predicting the impacts of AWB on TC activity. Zhang and Wang (2019) suggested that AWB over the western Atlantic has a stronger influence on TC activity than AWB farther east. Western Atlantic AWB activity has a negative correlation with the AMM (Zhang and Wang 2019) and the AMM's modulation of Caribbean precipitation anomalies. A positive phase of the AMM and increased precipitation over the Caribbean is typically associated with less frequent AWB. Drouard et al. (2013) and Zavadoff and Kirtman (2019) indicated that subtropical Pacific dynamics may influence Atlantic wave breaking via modulation of the Rossby wave train that propagates synoptic waves farther downstream. The results of these studies further suggest that dynamical oscillations such as the Pacific decadal oscillation (PDO) or the Pacific–North American pattern (PNA) can be used to assess wave breaking impacts on Atlantic convective events (Drouard et al. 2015; Zavadoff and Kirtman 2019).

Several studies have examined AWB's association with large-scale oscillations over the Atlantic region. Of note is the relationship between wave breaking and the North Atlantic Oscillation (NAO) in the boreal winter (hereafter winter). Benedict et al. (2004) indicated that sustained wave breaking in the winter could determine the phase of synoptic NAO variations. Intense AWB on the equatorward side of the subtropical jet stream displaces the jet northward and forces a positive phase of the NAO over the Atlantic, while cyclonic wave breaking along the poleward side of the jet forces an equatorward displacement of the jet stream and a negative phase of the NAO (Abatzoglou and Magnusdottir 2006a,b; Franzke et al. 2004).

Scaife et al. (2014) observed that the NAO, driven largely by internal atmospheric variability, has an intrinsic limit of predictability of around 3 weeks. However, there is also evidence of persistence beyond this limit through quasi-stationary regimes associated with the variability of the Azores high and Aleutian low (Czaja et al. 2003) or through persistent SST anomalies (Ogi et al. 2003). Persistence is defined here as the degree of dependence among successive values in time of a given phenomenon and is often a measure of the time interval between independent events (Wilks 2011). Given AWB's association with NAO variability, we hypothesize that there is a significant relationship between winter and summer wave breaking and investigate this hypothesis in this manuscript.

The purpose of our study is to assess winter–summer AWB variability and mechanisms by which we can infer possible AWB impacts on seasonal TC activity. Unlike previous studies, we show that AWB has not only a subseasonal relationship with the NAO but also a statistically significant seasonal relationship that has persistence on seasonal time scales. We also show that this seasonal AWB–NAO relationship has a strong association with TC activity. Including AWB impacts in seasonal Atlantic TC prediction helps explain anomalously suppressed seasons such as 2013 (Saunders et al. 2020) in which there is strong subtropical Atlantic forcing of the Atlantic environment. Depending on the intensity of wave breaking, AWB impacts may enhance or sustain current tropical environmental conditions. Alternatively, AWB may dominate tropical variability and TC activity when other large-scale drivers are relatively weak.

Jones et al. (2020) showed that subtropical AWB is associated with the second leading empirical orthogonal function (EOF) mode of 1979–2016 tropical VWS anomalies averaged over the Atlantic MDR, defined as 10°–30°N, 85°–20°W to include the subtropical Atlantic region. For the remainder of this manuscript, the EOF modes are also referred to as principal components (PCs). The subsequent AWB-shear (AWB-S) index correlated at −0.58 with accumulated cyclone energy (ACE; Bell et al. 2000) values during the peak season from

August to October and was statistically significant at the 95% level. As a single predictor regressed against July–September ACE values from 1979 to 2016, the AWB-S index exhibited a higher correlation compared with VWS anomalies averaged over the Atlantic MDR. The correlation between July–September ACE and the AWB-S index was $r = -0.57$, while the correlation between July–September ACE and VWS anomalies averaged over the Atlantic MDR was $r = -0.50$ (Jones et al. 2020). Additionally, the second principal component (PC2) associated with AWB improved the variance explained for ACE when combined with the leading principal component (associated mainly with ENSO) from $r^2 = 0.17$ to $r^2 = 0.27$.

In the sections that follow, we explore the relationship between winter and summer wave breaking episodes, how it manifests within the environment, and its consequent impact on seasonal TC predictability. The paper is organized as follows: section 2 outlines the data and methods used to further analyze the persistence of AWB impacts on the tropical environment. Section 3 describes the winter environmental precursors associated with summer AWB, while section 4 examines the use of a winter AWB-associated index as a predictor in an extended-range forecast model. Section 5 provides some concluding remarks.

2. Data and methods

a. Data

The TC analysis that follows uses ACE as the metric to classify overall seasonal activity levels. ACE is defined as the sum of the squares of the 6-hourly maximum wind speeds for each tropical and subtropical cyclone with 1-minute maximum sustained winds of at least 34 kt (1 kt $\approx$ 0.51 m s^{-1}; Bell et al. 2000). The index is calculated using the National Hurricane Center's best track database (HURDAT2; Landsea and Franklin 2013).

Environmental fields on both 6-hourly (0000, 0600, 1200, and 1800 UTC) and monthly time scales were obtained from the ECMWF's fifth-generation reanalysis (ERA5) dataset of the global atmosphere (Hersbach et al. 2020). Reanalysis data are currently available from 1 January 1979 to the present. The gridded ERA5 has a horizontal resolution of 0.25° × 0.25° for the atmosphere. Six-hourly potential vorticity and zonal wind anomaly fields used in the AWB detection algorithm were obtained with a resolution of 2.5° × 2.5° to remove small-scale disturbances (Postel and Hitchman 1999). We downloaded ERA5 data at a 2.5° × 2.5° resolution directly from the ECMWF's Climate Data Store (CDS) online platform. Monthly sea surface temperature anomalies at a 1° × 1° resolution were obtained from the National Oceanic and Atmospheric Administration's (NOAA) Optimum Interpolation Sea Surface Temperature version 2 (NOISSTv2) dataset from 1982 to 2019 (Reynolds et al. 2002). Anomalies for all fields are calculated relative to the 1981–2010 base period except for SST, which is calculated from a 1982–2010 base period. The period of study for the remainder of the manuscript is 1979–2019, but is restricted to 1982–2019 when using SST data.

Monthly indices were obtained for the NAO, ENSO, and the AMM. The NOAA Climate Prediction Center's (CPC) monthly NAO index is calculated from daily indices. The daily NAO index is defined as the leading rotated principal component of Atlantic 500-hPa height anomalies between 20° and 90°N (Barnston and Livezey 1987). Daily height anomalies are standardized by the 1981–2010 monthly mean and standard deviations from the principal component analysis. Variations in ENSO are assessed using the Niño-3.4 index (5°S–5°N, 170°–120°W) from 1982 to 2019 and are calculated from the NOISSTv2 dataset (Trenberth 2020). The AMM is defined as the principal leading mode of a maximum covariate analysis applied to Atlantic SSTs and 10-m surface wind speeds over the region 21°S–32°N, 74°W–15°E (Chiang and Vimont 2004; Kossin and Vimont 2007).

b. Methods

Following Jones et al. (2020), tropical zonal Atlantic VWS is defined as the difference between the 200- and 850-hPa zonal wind fields and averaged over the region 10°–30°N, 85°–20°W. We note that, while the zonal component of shear captures much of the structured variability in the total shear vector, the meridional component also contributes to a lesser degree. Anomalies were calculated relative to 1981–2010 to remove both the seasonal cycle and the climatological mean. The 1981–2010 period is the 30-yr climatological normal used in this study to assess anomalies within the seasonal environment (WMO 2017). An empirical orthogonal function (EOF) analysis was applied to July–September VWS fields from 1979 to 2019, and the second leading mode or principal component (PC2) previously associated with AWB activity was extracted, extending the time series of the second leading mode from the 1979–2016 period used in Jones et al. (2020). Composites using the variable fields mentioned in section 2b above are obtained for the 12 highest and the 12 lowest values of the 1979–2019 PC2 index. The period of study contains 41 sample years. We opt for 12 years to maximize the number of samples in each composite while preventing overlap.

We generated spatial correlations between the July–September PC2 index and seasonal sea level pressure (SLP), sea surface temperature (SST), and 850-hPa (U850) and 200-hPa (U200) zonal wind anomaly fields for the seasons January–March (JFM), April–June (AMJ), July–September (JAS), and October–December (OND). The JAS season is considered to be at zero lag (hereafter referred to as T), and the JFM, AMJ, and OND seasons are considered lags at $T - 2$, $T - 1$, and $T + 1$ seasons, respectively.

Statistical significance within the study is assessed in two ways. The significance of correlations is measured at the 95% confidence level corresponding to a p value < 0.05 based on a two-sided Student's t test. The statistical significance of the differences between the 12 high and 12 low composites are measured using the nonparametric Wilcoxon signed rank test. The Wilcoxon signed rank test categorizes the signed ranked differences into positive ($W+$) and negative ($W-$) groups, and calculates the sum of each category. If the difference between $W+$ and $W-$ metrics are larger than the threshold of

14 for $\alpha = 0.05$ and a sample size of 12, the null hypothesis that the differences are similar can be rejected (Wilks 2011).

For the present study, to assess the persistence of AWB's impact on the seasonal Atlantic environment, we projected an index of 200-hPa zonal wind anomalies onto the characteristic split-jet signal of AWB in the upper-level zonal wind field. The wave breaking or split-jet signal consists of a meridional tripole of zonal winds. This method of pattern projection, outlined in detail by Baldwin et al. (2009), was calculated using Eq. (1) below:

$$\mathrm{U200_{proj}} = \frac{Xe}{e^T e}, \tag{1}$$

where $\mathrm{U200_{proj}}$ is the index obtained from projecting the 200-hPa wind field X onto the flattened correlation pattern between the $\mathrm{AWB\text{-}S_{summer}}$ index and the wintertime upper-level zonal wind anomalies. The correlation pattern is denoted by e. The $\mathrm{U200_{proj}}$ index is then a pattern vector, much like the principal components from an EOF analysis, and indicates in standard deviations how similar the observed wintertime zonal upper-level wind field is to the correlation pattern. Alternatively, $\mathrm{U200_{proj}}$ is a measure of the presence of the summer AWB-S precursor signal within winter upper-level zonal winds. The index is used to further explore AWB's association with variations in 200-hPa zonal wind anomalies over the Atlantic region. The JAS AWB-S and projected indices are standardized over the 1981–2010 period. A more detailed description of the variability associated with the projected index is given in section 3.

A cross-spectrum analysis was applied with a Hanning window to examine shared frequencies (von Storch and Zwiers 1999) of variability in the monthly 1979–2019 $\mathrm{U200_{proj}}$, NAO and Niño-3.4 indices. Shared frequencies refer to periods of variability in which two variables are related within the spectral domain. To calculate the power spectrum of each index, the indices were separated into six chunks of 76 months with an overlap of 50% to avoid loss of information. The means of each chunk were removed to eliminate the zero-frequency signals. A chunk length of 76 months was chosen to maximize the number of chunks and degrees of freedom for the cross-spectrum analysis, while maintaining many samples in each chunk. A shared frequency was considered statistically significant at the 95% level if the coherence squared ($\mathrm{Coh^2}$) was above 0.45.

Last, we compare the skill of Colorado State University's (CSU) 2019 and 2020 early April statistical extended-range forecasts of seasonal ACE. Unlike the 2019 early April scheme, the most recent 2020 scheme comprises an AWB-S associated predictor (Klotzbach et al. 2019, 2020). The predictors are ranked based on the strength of their regression against ACE (via the F value) and the statistical significance of the regression strength (via the p value). The F value is the ratio of the mean sum of squares to the mean squared error (Wilks 2011) and measures whether an unrestricted model (e.g., a combination of predictors thought to be most appropriate for the data) performs better than a restricted model with the slope equal to zero. If the unrestricted model performs better than the restricted model, F is larger. The p value assesses how significant the F value is. The threshold for a statistically significant F value (F_{critical}) is 2.01 for a sample size $n = 41$ and is associated with a 90% significance level ($p = 0.1$).

A revised statistical model is created by selecting the top four predictors with the largest F value. The performance of the revised model is measured using the mean absolute error (MAE) and the explained variance (r^2) scores and is compared to the performance of the original early April statistical scheme.

c. Detecting AWB and AWB-associated VWS (AWB-S)

Wave breaking indices in this study were generated using an algorithm based on the techniques of Papin et al. (2020) and detailed in Jones et al. (2020). The algorithm calculates the potential vorticity streamer intensity (PVSI) from each PV anomaly detected. PVSI is defined as the standardized PV anomaly relative to a 6-hourly 1979–2019 climatological mean and is integrated over the areal extent of the PV streamer detected along the 2-PVU (1 PVU $\equiv 10^{-6}$ K kg^{-1} m^2 s^{-1}) contour on the 350-K isentropic surface. The algorithm detects more than two consecutive points along the 2-PVU contour with an eastward (west to east) PV gradient ($\partial \mathrm{PV}/\partial x > 0$) and a reversal in the poleward meridional PV gradient ($\partial \mathrm{PV}/\partial y < 0$) for the upstream edge of the PV tongue. The opposite criteria is applied for detection of the downstream edge ($\partial \mathrm{PV}/\partial x < 0, \partial \mathrm{PV}/\partial y > 0$) (Abatzoglou and Magnusdottir 2006b; Papin et al. 2020). As done in Jones et al. (2020) and Papin et al. (2020), once the points outlining the PV tongue are identified, a line connects the two endpoints to capture the PVS polygon and as much of the PVS area as possible.

In addition to the count and intensity, the same detection algorithm collects the VWS anomalies from the zonal shear field at consecutive points along the downstream edge of each detected PV streamer (Jones et al. 2020). We note that the shear patterns associated with AWB can extend well into the tropics, producing large VWS anomalies along both the upstream and downstream edges. Correlations of the sum of the downstream and upstream AWB-S anomalies with VWS averaged over the MDR (not shown) are similar to correlations for the downstream AWB-S only. Therefore, we opt to use the downstream AWB-S in calculating the AWB-S indices. The VWS anomaly is then summed to obtain an index of AWB-associated VWS (AWB-S). The AWB-S index can be used to examine the level of sustained impact to the tropical environment by intense wave breaking.

3. Evidence for a strong winter–summer AWB connection

a. PC2 correlations with the seasonal environment

Figure 2 shows correlations, significant at the 95% confidence level based on the two-sided Student's t test, between the 1979 and 2019 JAS second leading mode of tropical Atlantic VWS (PC2) and seasonal SLP, SST, U850, and U200 anomaly

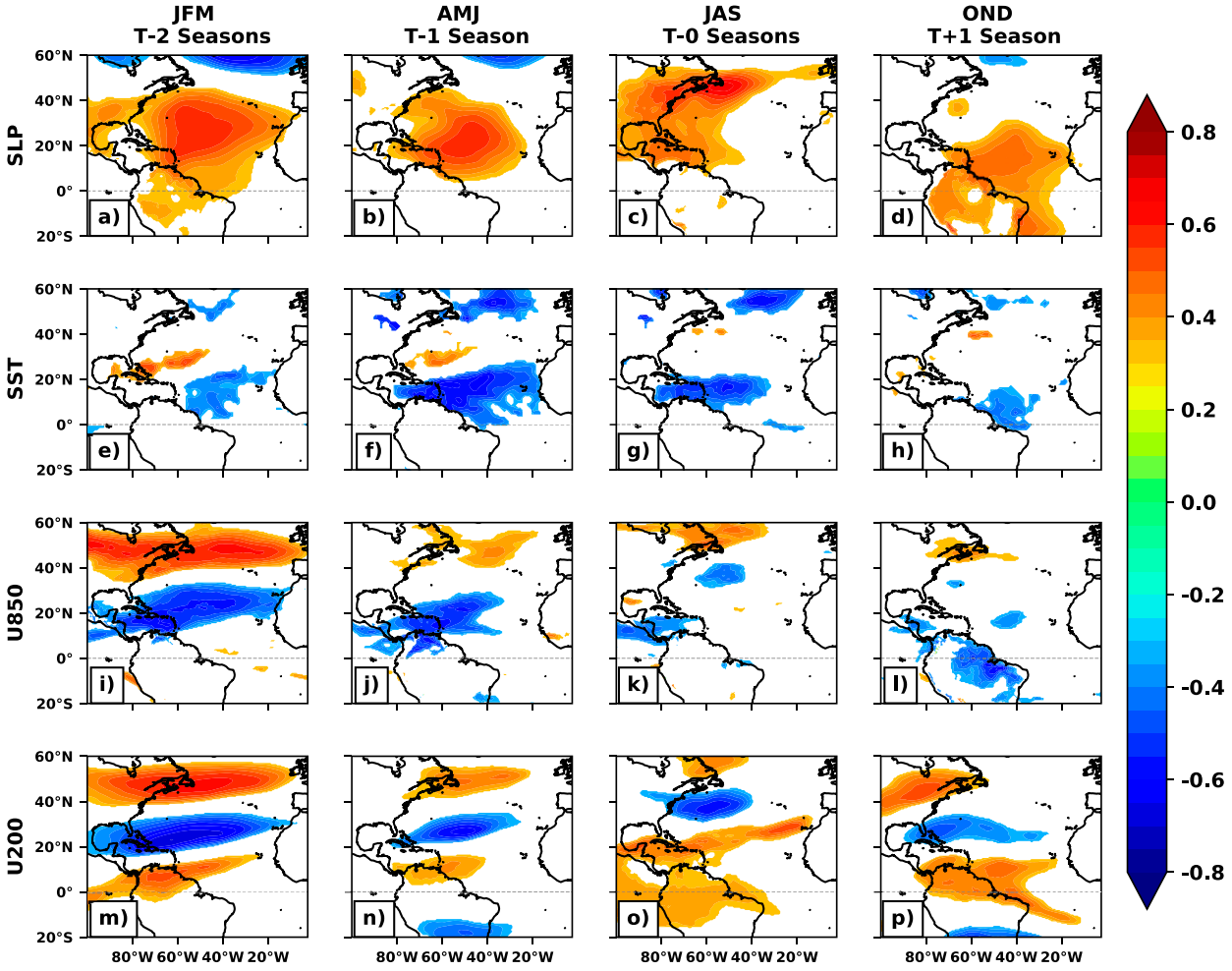

FIG. 2. Spatial correlations between the second leading mode (PC2) of July–September (zero lag, $T - 0$ seasons) 1979–2019 Atlantic vertical wind shear (10°–30°N, 85°–20°W) and seasonal anomalies in (a)–(d) SLP, (e)–(h) SST, and (i)–(l) 200- and (m)–(p) 850-hPa zonal winds for January–March ($T - 2$ seasons), April–June ($T - 1$ season), and October–December ($T + 1$ season). Only correlations statistically significant at the 95% confidence level are shaded.

fields. AWB—identified by upper-level anticyclonically sheared wind anomalies that are hereafter referred to as the wave breaking signal—is associated with higher SLP anomalies (Figs. 2a–d) and lower SST anomalies (Figs. 2e–h) across the tropical and subtropical Atlantic region. These associations are evident in the concurrent environmental fields (Figs. 2c,g,k,o). We further observe that summer AWB impacts, quantified using the PC2 index, have strong associations with the seasonal environments preceding and following JAS. Of note, several JFM environmental fields correlate strongly with JAS AWB. Of particular note are the winter U850 and U200 patterns (see Figs. 2i,m) that suggest a physical link between winter and summer AWB.

In Figs. 2a–d, summer AWB activity shows strong positive correlations with Atlantic SLP anomalies, meaning SLP anomalies increase over the central Atlantic with more intense wave breaking. The correlation pattern is consistently strong across the tropical and subtropical Atlantic region from JFM through OND. This result is consistent with previous studies of winter AWB activity. Abatzoglou and Magnusdottir (2006b) and Bowley et al. (2019) found correlations > 0.5 between winter AWB and the NAO. There is a noticeable shift in the position of the SLP correlation maximum from the eastern Atlantic during the boreal winter and spring to the western Atlantic during JAS. Increased SLP anomalies over the Caribbean and northeastern U.S. coast indicate strong AWB activity. In OND, the signal weakens over the western Atlantic and migrates back toward the eastern Atlantic. The eastern position of the SLP signal generally indicates weaker AWB (Papin 2017; Papin et al. 2020). The seasonal AWB–SLP correlations show that there are robust precursor signals that may be used to predict summer AWB-associated shear impacts. These strong signals within SLP may also suggest that summer AWB activity is in some way connected to the state of the NAO in preceding seasons via its modulation of large-scale SLP anomalies.

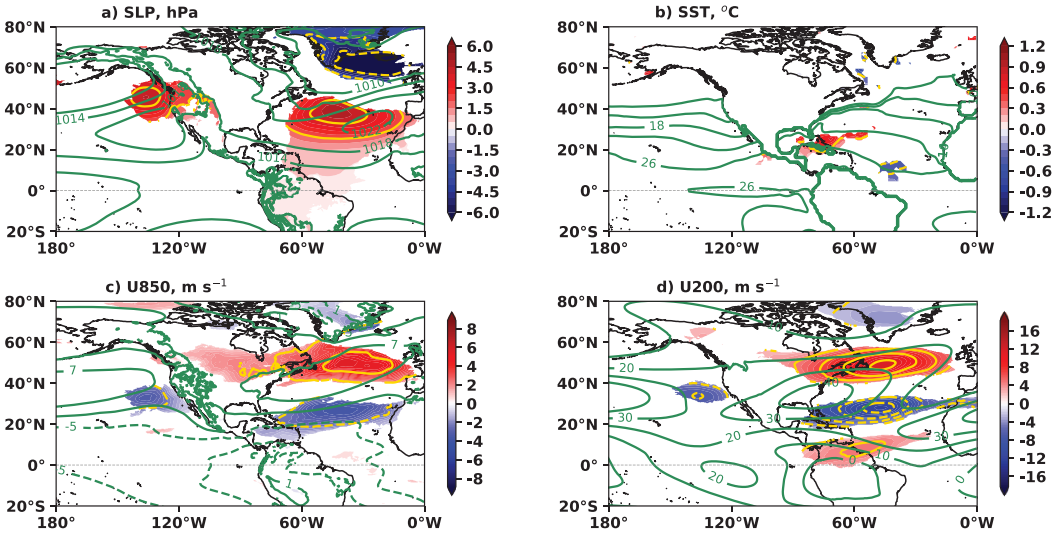

FIG. 3. Differences in January–March ($T - 2$ seasons) composites of the 12 highest values vs 12 lowest values for the second leading mode of July–September ($T - 0$ seasons) VWS variability (PC2) for (a) sea level pressure (SLP; hPa), (b) sea surface temperatures (SST; °C), (c) 850-hPa U (U850; m s^{-1}), and (d) 200-hPa U (U200; m s^{-1}). Shaded regions indicate composite differences statistically significant at the 95% confidence level based on the Wilcoxon signed rank test. The dark green contours indicate the JFM climatological mean for each variable. Gold contours highlight anomalies at intervals of 2 hPa, 0.4°C, and 2 m s^{-1} for SLP, SST, and both U850 and U200, respectively.

Figures 2e–h show that the JAS PC2 index is anticorrelated with tropical Atlantic SSTs. Above-normal AWB activity is associated with negative SST anomalies along the downstream edge of a PV streamer and positive SST anomalies along the upstream edge (Zhang et al. 2017; Zhang and Wang 2019; Papin et al. 2020). Zhang and Wang (2019) show that these negative SST anomalies are predominantly due to an anomalous low-level circulation imposed by sustained AWB that also facilitates the low-level advection of warm tropical air poleward and cool midlatitude air equatorward. Negative SST anomalies are evident in the JFM and AMJ SST correlation fields. There is also a second region of negative correlations in the subpolar gyre region, collocated with the correlation observed in U850. Correlations with Atlantic SSTs are also stronger in AMJ, indicating that the AWB-SST signal is a response to intense and persistent signals during the previous season.

Figure 3 shows the differences in composites of JFM environmental fields for the 12 highest values versus the 12 lowest values of the JAS PC2 index. The highest composites occur in 1990, 2018, 2003, 2015, 1994, 2002, 2014, 1984, 1989, 2013, 1992, and 2001; the lowest composites occur in 2005, 2010, 1999, 1998, 1987, 1991, 2004, 1981, 1997, 2011, 1980, and 2006. The "highest" composite years are listed in descending order from the highest PC2 value while the "lowest" composite years are listed in ascending order from the lowest PC2 value. Winters with the highest values show signatures of wave breaking. Figure 3a displays two pronounced regions of high SLP anomalies, indicative of wave breaking over the Atlantic and along the western U.S. coast. The SLP composite is also indicative of a prominent positive NAO for high values of PC2. A positive NAO phase has been associated with an increase in subtropical Atlantic AWB in previous studies (Benedict et al. 2004; Woollings et al. 2008). Winters with high JAS AWB activity hint at a horseshoe pattern with positive SST anomalies in the subtropical Atlantic and negative SST anomalies in the tropical MDR (Fig. 3b). This horseshoe pattern becomes more apparent and statistically significant during AMJ (Fig. 2f). Figures 3c and 3d are dominated by wave breaking. This result suggests that for years with enhanced summer wave breaking, there was also enhanced wave breaking in the preceding winter season. In the JFM periods where JAS PC2 was highest, the NAO averaged 0.35 standard deviations, whereas in the 12 JFM periods where JAS PC2 was lowest the NAO averaged −0.44 standard deviations. This difference hints at the significant role that the NAO plays in preconditioning the atmospheric environment for significant AWB during JAS.

Figure 4 shows composites of JFM 850- and 200-hPa geopotential height anomalies for the 12 highest versus the 12 lowest values for the JAS PC2 index. For years with pronounced summer AWB, there is a poleward-shifted subtropical jet and a low-level subtropical high indicative of an anomalous anticyclonic circulation over the Atlantic region. Both features are associated with increased winter wave breaking. The composite of the 12 highest height years also suggests that above-normal summer AWB is associated with a positive-phase winter NAO. By contrast, in years with less summer AWB, 200-hPa height anomalies show little indication of anticyclonically sheared wave breaking. Instead, the 850-hPa subtropical high is anomalously weak (e.g., anomalously low pressure) due to an equatorward shift of the subtropical jet. An equatorward displacement of the subtropical jet is indicative of cyclonic wave breaking on the poleward

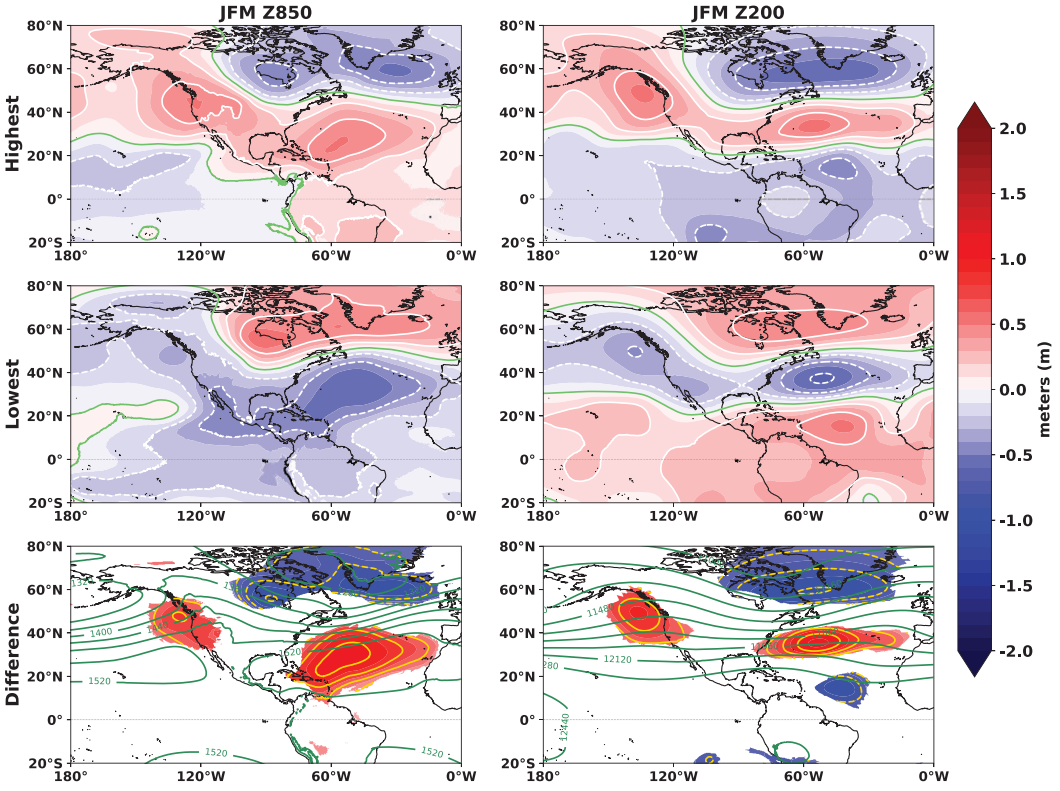

FIG. 4. Composites of January–March ($T - 2$ seasons) (left) 850- and (right) 200-hPa geopotential height anomalies (in m) for (top) the 12 highest values vs (middle) the 12 lowest values for the July–September ($T - 0$ seasons) PC2 index. White contours (and gold contours in bottom panels) indicate intervals of 0.2 m; light green contours in the top and middle rows highlight the zero anomaly contour. (bottom) Shaded regions indicate composite differences statistically significant at the 95% confidence level based on the Wilcoxon signed rank test. Dark green contours in the bottom row highlight the climatological mean.

side of the jet and a negative phase of the NAO. The most significant changes in the composites are situated over the Atlantic and the western U.S. coast, indicating that the dynamical difference between the composites is likely due to wave breaking and associated variations in the NAO. We also note that seasonal mean fields show a smooth spatial pattern that prevents us from observing actual Rossby wave breaking (RWB) events.

Similar patterns are observed for the composites of AMJ 850- and 200-hPa geopotential height anomalies (Fig. 5). The composite difference displays a low-level high over the subtropical Atlantic, similar to a positive phase of the NAO, when high values of the JAS PC2 index are present. At upper levels, the anticyclonically sheared signal is less pronounced in the AMJ composites (in contrast to the AMJ composites in Fig. 4) and is associated with a prominent low-level high over the subtropical Atlantic region. We note that the lack of an AWB signal in upper-level height anomalies may be due to seasonal shifts in the vertical location relative to the 350-K surface used to evaluate AWB (Kunz et al. 2015). Although there are some differences at upper levels for the tropical and extratropical regions, composite differences in the subtropical Atlantic are relatively weak.

b. The $U200_{proj}$ index

As described in section 3b, the strong correlation pattern between JAS AWB-S_{summer} index and JFM zonal wind anomalies (shown in the inset of Fig. 6) was projected onto an index of JFM Atlantic 200-hPa zonal wind speeds averaged over 5°–80°N, 80°–10°W using Eq. (1) and the method outlined in section 2b. Therefore, the subsequent index ($U200_{proj}$) is a measure of the strength of each year's winter–summer relationship. We note here that AWB activity shows strong variability in multiple environmental fields that likely contain a significant winter–summer AWB correlation (e.g., the SLP anomaly fields). For this study, we focus on the evolving pattern of variability in the 200-hPa zonal wind field.

Figure 6 compares the $U200_{proj}$ index to the summer AWB-S and PC2 indices. The correlations between these three indices are outlined in Table 1. For the period 1979–2019, the $U200_{proj}$ index has correlations of $r = 0.66$ and $r = 0.45$ with JAS PC2 and AWB-S_{summer}, respectively, and illustrates that the winter $U200_{proj}$ index is a good indicator of summer AWB-S variability. Correlations between the $U200_{proj}$ index and the August–October environment are given in Fig. 7, which indicates that the index's associations are particularly significant in the Caribbean region. The $U200_{proj}$ index is

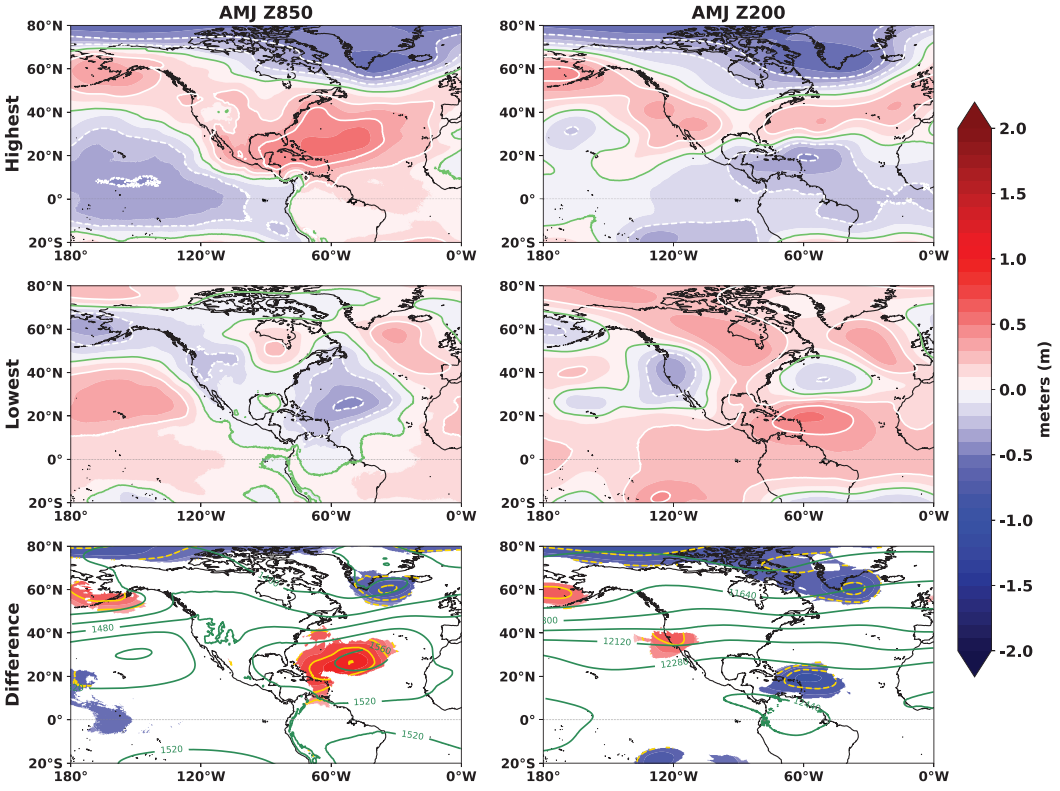

FIG. 5. Composites of April–June ($T - 1$ season) (left) 850- and (right) 200-hPa geopotential height anomalies (in m) for (top) the 12 highest values vs (bottom) the 12 lowest values for the July–September ($T - 0$ seasons) PC2 index. White contours (and gold contours in bottom panels) indicate intervals of 0.2 m; light green contours in the top and middle rows highlight the zero anomaly contour. (bottom) Shaded regions indicate composite differences statistically significant at the 95% confidence level based on the Wilcoxon signed rank test. Dark green contours in the bottom row highlight the climatological mean.

associated with anomalously high SLPs, anomalously low SSTs, and anomalously strong VWS in the Caribbean region. All of these conditions typically suppress Atlantic hurricane activity (Jones et al. 2020). A prominent El Niño signal is also evident in the SST correlations. Jones et al. (2020) and Papin (2017) have shown that AWB activity has a positive correlation with ENSO. The patterns shown in Fig. 7 are consistent with the current understanding of AWB's environmental impacts.

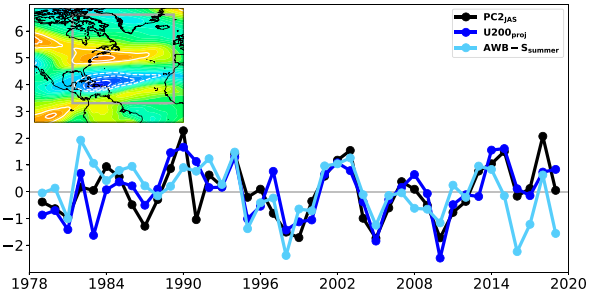

FIG. 6. Time series comparison of the July–September ($T - 0$ seasons) AWB-S index (AWB-S_{summer}), the second leading mode of Atlantic VWS (PC2), and the $U200_{proj}$ index for the period 1979–2019. All indices are standardized over the period 1981–2010. The inset shows the correlation pattern between the AWB-S_{summer} index and JFM 200-hPa anomalies. Winter 200-hPa zonal wind anomalies are projected against the inset pattern to generate $U200_{proj}$.

c. The role of the NAO in AWB-S persistence

Figure 8a shows the monthly time series of $U200_{proj}$, NAO, and ENSO indices from 1979 to 2019. At zero lag, $U200_{proj}$

TABLE 1. Correlation coefficients between 1979 and 2019 July–September PC2 and (AWB-S_{summer}) AWB shear indices, the $U200_{proj}$ index, and 1982–2019 January–March subtropical 200-hPa zonal wind anomalies ($U200_{subtropical}$) used as the second predictor in the 2020 CSU early April statistical scheme. Correlations statistically significant at the 95% significance level are highlighted in boldface.

	PC2	AWB-S_{summer}	$U200_{proj}$	$U200_{subtropical}$
PC2	—	**0.55**	**0.66**	**−0.51**
AWB-S_{summer}	**0.55**	—	**0.45**	**−0.40**
$U200_{proj}$	**0.66**	**0.45**	—	**−0.81**
$U200_{subtropical}$	**−0.51**	**−0.40**	**−0.81**	—

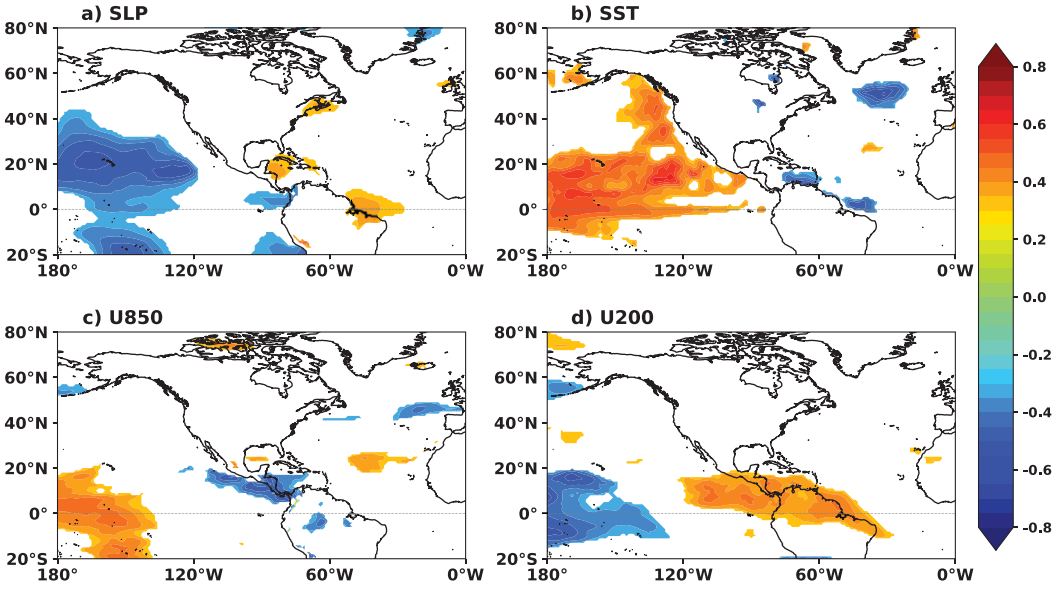

FIG. 7. Pearson correlation coefficients between the $U200_{proj}$ index and August–October (a) SLP, (b) SST, (c) U850, and (d) U200 fields for the period 1979–2019. The shading indicates statistical significance at the 95% level.

has insignificant correlations with the NAO ($r_{NAO} = 0.15$) and ENSO ($r_{Niño3.4} = 0.06$). The results of the cross-spectrum analyses shown in Fig. 8b indicate that $U200_{proj}$ and NAO share a period of 3 months with a coherence of 0.49, significant at the 95% confidence level. The quadrature spectrum shows a positive phase difference of 1 month when the $U200_{proj}$ leads the NAO, as shown in Fig. 8c. Therefore, the strong winter AWB tends to precede a positive NAO by 1 month. The cross-spectrum analysis shows that $U200_{proj}$ is associated with low-frequency variations in the NAO. Furthermore, the persistence of AWB-associated 200-hPa zonal wind anomalies observed earlier in section 3a is facilitated by AWB's forcing of the NAO on seasonal time scales. This result is consistent with $U200_{proj}$ being a projection of the subtropical component of VWS variability (PC2). The result is also consistent with earlier observations by Benedict et al. (2004) and Woollings et al. (2008) of AWB forcing low-frequency variations in the NAO.

The phase of the NAO has previously been linked to variations in the location and strength of the Atlantic jet stream (Martius et al. 2008; Woollings et al. 2008, 2010; Zhang et al. 2016). Positive NAO anomalies reinforce the anticyclonically sheared circulation that triggers further AWB in the vicinity of the subtropical high, while negative anomalies are associated with more cyclonically sheared flow and a decline in AWB, leading to more cyclonic wave breaking (Martius et al. 2008). While few studies have examined the NAO and AWB during AMJ, we infer that positive (negative) AMJ geopotential height anomalies associated with positive (negative) winter AWB-S (Figs. 4 and 5) encourage more (less) AWB in subsequent seasons.

4. AWB inclusion in an early April extended-range forecast for Atlantic hurricane activity

In section 3, we show that winter AWB activity can be used to estimate the intensity of summer wave breaking activity. We also show that abnormally strong winter AWB activity can force a positive phase of the NAO that lags AWB activity by a month. Franzke et al. (2004) suggested that the AWB-forced NAO anomalies may be sustained well into the summer by continued wave breaking throughout the year (see Fig. 3). We have therefore interpreted the $U200_{proj}$ index to be a quantitative indication of the persistence of AWB-forcing on upper-level winds via the strength of the winter–summer link. Table 2 shows that $U200_{proj}$ has statistically significant correlations of $r = -0.35$ and $r = -0.41$ with ACE and the number of hurricanes, respectively. These results suggest that the perceived winter–summer persistence in AWB activity via forcing of the low-frequency NAO variability could be used to provide additional skill to extended-range forecasts of seasonal TC activity, particularly for seasons with unusually suppressed TC activity like the 2013 season.

The JFM $U200_{proj}$ index's contribution to skill is best demonstrated with CSU's 2020 early April forecast scheme (Klotzbach et al. 2020). Below, we compare the performance of the previous 2019 CSU early April forecast statistical scheme to that of the revised 2020 early April scheme (Klotzbach et al. 2019). The 2019 forecast scheme is hereafter referred to as the original model, and the 2020 forecast scheme is referred to as the revised model. Table 3 lists the statistical predictors used in Colorado State University's 2019 early April extended range forecast scheme, the regions over which the predictors were averaged, and their correlation with June–November ACE (Klotzbach et al. 2019).

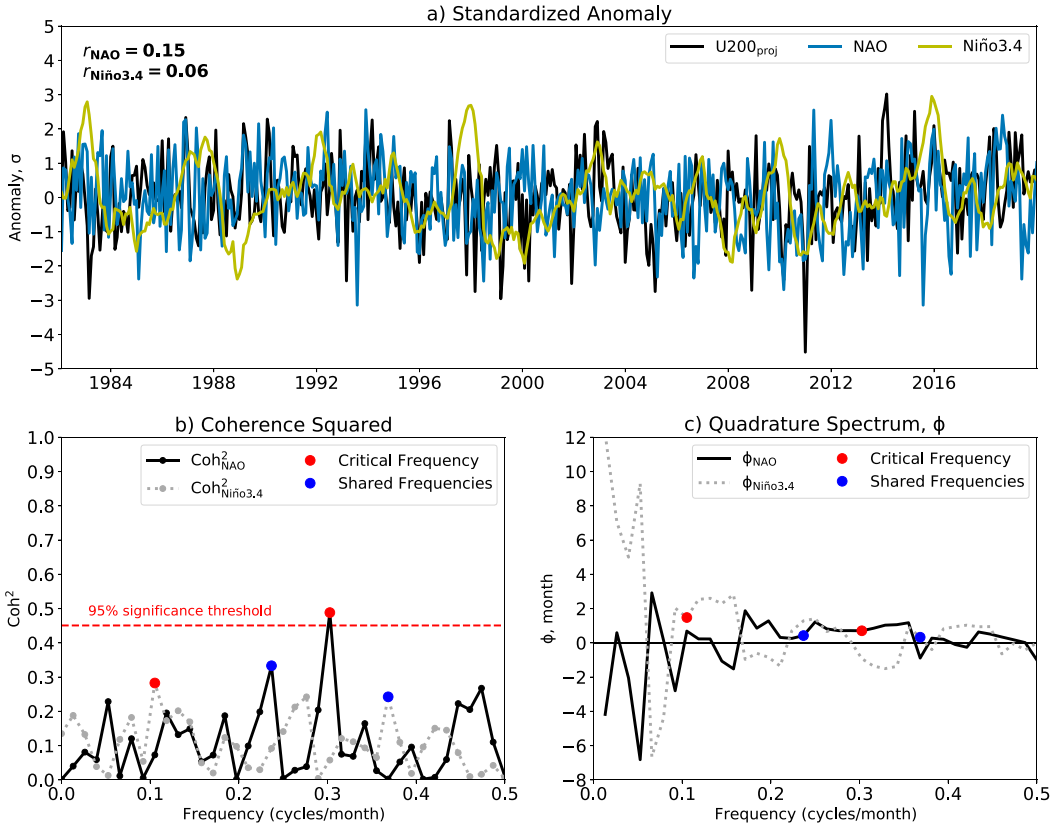

FIG. 8. Cross-spectrum analyses between standardized monthly variations in the $U200_{proj}$ index, NAO, and Niño-3.4 indices for the period 1979–2019. (a) Time series plots of monthly standardized $U200_{proj}$ (black), NAO (blue), and Niño-3.4 (green) indices. (b) The coherence squared between $U200_{proj}$ and NAO (Coh^2_{NAO}, solid black line) and $U200_{proj}$ and Niño-3.4 ($Coh^2_{Niño\ 3.4}$, dashed gray line). The critical frequency at which the coherence squared is strongest in each spectrum is highlighted by the red dot, while shared frequencies are shown in blue. The threshold for 95% significance is highlighted by the dashed red line. (c) Phase difference between the $U200_{proj}$ index and the NAO (solid black line) and Niño-3.4 (dashed gray line) indices. The red dot highlights the phase difference at the critical frequency. Positive (negative) phase differences indicate that $U200_{proj}$ leads (lags) the climate indices.

The original statistical scheme includes the following as predictors: January–March SSTs over the North Atlantic region, March Atlantic SLP, February–March Pacific SLP, and forecast values of the September Niño-3 index from the ECMWF SEAS5 dynamical model (Table 3). Anomalously high Atlantic SSTs in January–March are generally associated with the positive phase of the AMM and an active TC season (Klotzbach and Gray 2008). Higher SSTs are also associated with weaker lower and upper tropospheric winds, weaker

TABLE 2. Correlation coefficients between 1979 and 2019 June–November metrics of TC activity [accumulated cyclone energy (ACE), total number of named storms, total number of hurricanes, and total number of hurricane days] and the July–September ($AWB\text{-}S_{summer}$) AWB shear indices, and the $U200_{proj}$ index. Values highlighted in boldface indicate correlations statistically significant at the 95% level.

	$AWB\text{-}S_{summer}$	$U200_{proj}$
ACE	**−0.61**	**−0.40**
Named storms	**−0.54**	**−0.31**
Major hurricanes	**−0.60**	**−0.43**
Major hurricane days	**−0.51**	−0.30
Hurricanes	**−0.56**	**−0.46**
Hurricane days	**−0.51**	−0.30

TABLE 3. List of predictor domains for the 2019 CSU early April statistical scheme, and the correlation r_{ACE} between each predictor and 1982–2019 accumulated cyclone energy (ACE).

Predictors	Region	r_{ACE}
January–March Atlantic SSTs (predictor 1)	5°S–35°N, 40°–10°W	0.42
March Atlantic SLP (predictor 2)	20°–40°N, 35°–20°W	−0.20
February–March Pacific SLP (predictor 3)	20°–5°S, 120°–85°W	0.25
Predicted September Niño 3 (predictor 4)	5°S–5°N, 150°–90°W	−0.48

TABLE 4. List of predictor domains for the 2020 CSU early April statistical scheme and the correlation r_{ACE} between each predictor and 1982–2019 accumulated cyclone energy (ACE).

Predictors	Region	r_{ACE}
January–March Atlantic SST	5°S–50°N, 40°–10°W	0.56
January–March $U200_{subtropical}$	17.5°–27.5°N, 60°–20°W	0.45
February–March Coral Sea SST	20°S–0°, 145°–170°E	0.52

VWS, and anomalously low sea level pressure over the Atlantic MDR during August–October. High SLP anomalies are associated with a stronger Azores high and lower SSTs in the subtropics which is an indication of a less favorable environment for TC development. The third predictor, February–March southeastern tropical Pacific SLPs, is associated with lower SLP anomalies, weaker low-level wind anomalies over the Atlantic MDR and Caribbean regions and lower SSTs in the eastern equatorial Pacific during August–October. These are conditions consistent with a La Niña event. The fourth predictor, predicted September Niño-3 SSTs, are an indicator of the state of ENSO during the peak hurricane season and are consequently negatively correlated with TC activity ($r = -0.48$). Higher Niño-3 SSTs are associated with El Niño conditions and an increase in VWS over the Atlantic, while lower Niño-3 SSTs are associated with La Niña conditions and a reduction in VWS.

Table 4 lists the three statistical predictors used for the revised early April model. The revised statistical scheme includes the JFM tropical–subtropical eastern Atlantic SSTs retained from the original scheme, JFM subtropical Atlantic 200-hPa zonal winds, and February–March Coral Sea SSTs. The new JFM subtropical Atlantic U200 predictor correlates well with the $U200_{proj}$ index for the period 1982–2019 ($r = -0.81$; shown in Table 1) and is associated with a weaker than normal Azores high, weaker trade winds, and higher SSTs over the Atlantic MDR. Higher than normal Coral Sea SSTs are typically associated with lower pressure over the western Pacific and higher pressure over the eastern Pacific. This pressure gradient pattern favors enhanced tropical Pacific trade winds, inhibiting El Niño development. The 2020 early April statistical scheme has a correlation of $r = 0.66$ with 1982–2020 ACE, whereas the ACE correlation for the early April 2019 scheme is $r = 0.54$ for 1982–2020.

Figure 9 shows the individual F values of each predictor in the original and revised forecast schemes. The F and p values are determined from the correlation between ACE and each individual predictor. Therefore, the statistical values measure the strength of the relationship between each predictor and ACE. Here, we consider the F value of the predictor to be statistically significant if $F_{critical} > 2.01$, yielding a $p < 0.1$. The predictors of the revised forecast scheme all outperform those of the original scheme. The JFM Atlantic SST predictor has the highest F value with $F = 14$ and $F = 17$ for the original and revised schemes, respectively. In the revised model, the JFM U200 has an F value of 9 while the February–March Coral Sea SST has an F value of 14. Figure 10 compares the predictions made by the original and revised statistical models for the years 1982–2020. Both schemes were trained on 1982–2010 ACE values and then tested on the period 2011–20. The MAE and r^2 scores for the revised 2020 scheme show strong improvements over the original for both the training and testing periods. The original scheme fails to explain any variance in ACE for the 2011–20 period.

5. Discussion and conclusions

Recent studies have shown that subtropical anticyclonic wave breaking (AWB) influences seasonal North Atlantic tropical cyclone (TC) activity via AWB's forcing of tropical vertical wind shear (VWS) (Zhang et al. 2016, 2017; Papin et al. 2020). An index representing summer AWB-associated environmental anomalies provides one way of quantifying

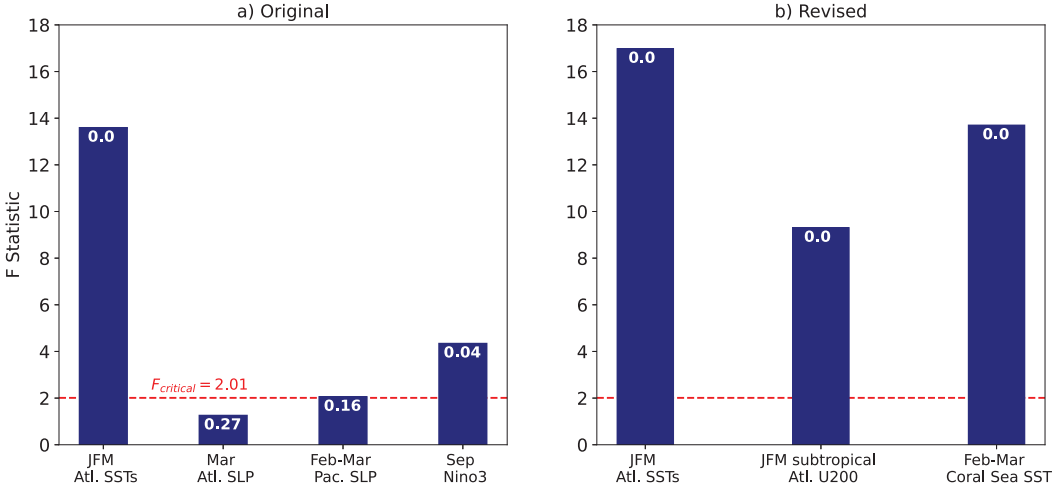

FIG. 9. F-value statistic for each early April predictor in the (a) original CSU 2019 and (b) revised 2020 statistical Atlantic hurricane forecast models. Each predictor is labeled with the associated p value. Statistically significant F values exceed $F_{critical} = 2.01$ for $p = 0.1$.

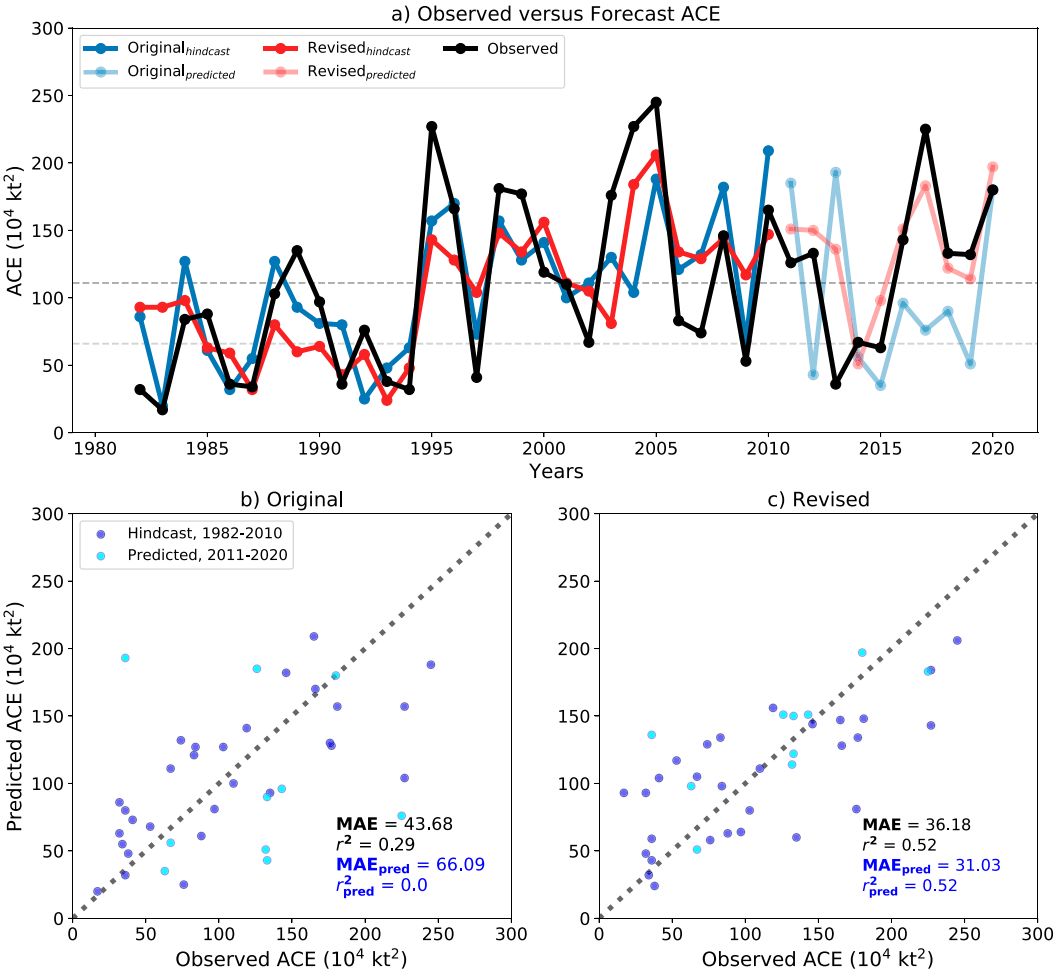

FIG. 10. Linear regression performance of the original CSU 2019 early April statistical scheme and the revised CSU 2020 early April statistical scheme. (a) Seasonal predictions of ACE based on the original 2019 early April statistical scheme (blue) and the revised 2020 scheme (red) vs observed ACE values (in black) from 1982 to 2020. Solid lines indicate the hindcast/training period from 1982 to 2010; transparent lines indicate the testing period from 2011 to 2020. Dark gray lines indicate near-normal activity between 66×10^4 and 111×10^4 kt^2. Levels exceeding 111×10^4 kt^2 are classified as above normal while levels less than 66×10^4 kt^2 are classified as below normal. These definitions are based on NOAA's Atlantic hurricane season classification criteria as of 2020 (CPC 2020). (b) Scatterplots of ACE forecasted by the original 2019 forecast scheme. (c) Scatterplots of ACE forecasted by the revised 2020 forecast scheme. The mean absolute error (MAE) and variance explained (r^2) is given for the full 1982–2020 period (MAE, r^2) and the training period 2011–20 (MAE$_{pred}$, r^2_{pred}).

AWB's impact on the Atlantic MDR, adding skill to seasonal predictions of TC activity (Jones et al. 2020). In this study, we examine the use of the strong winter environment/summer AWB–shear link to assess the predictability of AWB impacts on seasonal TC activity and show that including the dynamical effects of AWB is useful in seasonal TC predictions. The key findings of our study are as follows:

1) There is a strong association between winter and summer AWB shear impacts. Correlations significant at the 95% confidence level between the July–September (JAS) AWB-shear index and the January–March (JFM) 200-hPa zonal wind field show anticyclonically sheared wind anomalies that indicate wave breaking.
2) The strength of the winter–summer AWB relationship is an indication of wave breaking–induced NAO anomalies. Continuous wave breaking sustains seasonal NAO anomalies and provides a physical explanation for persistence in seasonal AWB shear impacts.
3) Potential impacts of summer wave breaking on TC activity can be estimated by projecting an index of January–March 200-hPa zonal wind anomalies onto the winter–summer AWB relationship, denoted here as $U200_{proj}$.

4) The $U200_{proj}$ index is significantly correlated at −0.35 with ACE and 0.45 with summer AWB-shear indices. The revised early April statistical seasonal hurricane forecast model from CSU including an index closely related to $U200_{proj}$ improves upon CSU's 2019 early April extended-range statistical forecast from 1982 to 2020.

The results of this study show that AWB-associated 200-hPa zonal wind anomalies are persistent within the environment through their low-frequency covariability with the quasi-stationary NAO. The low-frequency AWB–NAO relationship explains the strong correlations we observed between winter AWB and summer AWB shear impacts and improves the extended-range skill of seasonal TC predictions. We also suspect that the $U200_{proj}$ index can account for above- or below-normal subtropical Atlantic TC variability and offer added skill in years with ENSO-neutral conditions where the predictability of the large-scale environment is reduced (Saunders et al. 2020; Wood et al. 2020).

One limitation of the $U200_{proj}$ index is due to the strong nonlinear component of AWB variability. This means that the winter–summer link and the $U200_{proj}$ index do not always account for the magnitude of summer wave breaking impacts. The $U200_{proj}$ index only accounts for 16% of the explained variance in the summer AWB-shear index and may be underwhelming as a predictor in multiple linear regressions alongside the strong forcing from ENSO-related predictors. This limitation raises a key question about TC prediction: *Are current schemes sophisticated enough to pick up the subtle dynamical forcing (e.g., for AWB) that may drive the large-scale atmospheric circulation, especially during ENSO-neutral conditions?* We intend to investigate the use of nonlinear regression techniques for Atlantic TC prediction in future work to answer this question.

Acknowledgments. This research was supported by the Office of Naval Research Award N000141613033, the G. Unger Vetlesen Foundation, and the Fulbright Foreign Student Program. We also thank the editor and the three anonymous reviewers for their comments and suggestions that helped to improve our manuscript. Thanks also to Eric Maloney for providing valuable feedback on this study.

Data availability statement. Data generated and analyzed for this study are freely available in the Mendeley Data Repository ("Anticyclonic Rossby wave breaking (AWB)-associated vertical wind shear anomalies, 1979–2019") at https://doi.org/10.17632/cmfbkdz4f6.1. All climate indices were sourced from the National Oceanic and Atmospheric Administration Physical Sciences Laboratory (PSL) Climate Indices online database freely accessible at https://psl.noaa.gov/data/climateindices/list/. The ERA5 data are freely available from the ECMWF's Climate Data Store (CDS) online platform at https://cds.climate.copernicus.eu/. The NOAA Optimum Interpolation Sea Surface Temperature version 2 dataset can be accessed at https://psl.noaa.gov/data/gridded/data.noaa.oisst.v2.html.

REFERENCES

Abatzoglou, J. T., and G. Magnusdottir, 2006a: Opposing effects of reflective and nonreflective planetary wave breaking on the NAO. *J. Atmos. Sci.*, **63**, 3448–3457, https://doi.org/10.1175/JAS3809.1.

——, and ——, 2006b: Planetary wave breaking and nonlinear reflection: Seasonal cycle and interannual variability. *J. Climate*, **19**, 6139–6152, https://doi.org/10.1175/JCLI3968.1.

Aiyyer, A. R., and C. Thorncroft, 2006: Climatology of vertical wind shear over the tropical Atlantic. *J. Climate*, **19**, 2969–2983, https://doi.org/10.1175/JCLI3685.1.

Bach, E., S. Motesharrei, E. Kalnay, and A. Ruiz-Barradas, 2019: Local atmosphere–ocean predictability: Dynamical origins, lead times, and seasonality. *J. Climate*, **32**, 7507–7519, https://doi.org/10.1175/JCLI-D-18-0817.1.

Baldwin, M. P., D. B. Stephenson, and I. T. Jolliffe, 2009: Spatial weighting and iterative projection methods for EOFs. *J. Climate*, **22**, 234–243, https://doi.org/10.1175/2008JCLI2147.1.

Barnston, A. G., and R. E. Livezey, 1987: Classification, seasonality and persistence of low-frequency atmospheric circulation patterns. *Mon. Wea. Rev.*, **115**, 1083–1126, https://doi.org/10.1175/1520-0493(1987)115<1083:CSAPOL>2.0.CO;2.

Bell, G. D., and Coauthors, 2000: Climate assessment for 1999. *Bull. Amer. Meteor. Soc.*, **81**, S1–S50, https://doi.org/10.1175/1520-0477(2000)81[s1:CAF]2.0.CO;2.

Benedict, J. J., S. Lee, and S. B. Feldstein, 2004: Synoptic view of the North Atlantic Oscillation. *J. Atmos. Sci.*, **61**, 121–144, https://doi.org/10.1175/1520-0469(2004)061<0121:SVOTNA>2.0.CO;2.

Bowley, K. A., J. R. Gyakum, and E. H. Atallah, 2019: A new perspective toward cataloging Northern Hemisphere Rossby wave breaking on the dynamic tropopause. *Mon. Wea. Rev.*, **147**, 409–431, https://doi.org/10.1175/MWR-D-18-0131.1.

Camargo, S. J., and A. H. Sobel, 2010: Revisiting the influence of the quasi-biennial oscillation on tropical cyclone activity. *J. Climate*, **23**, 5810–5825, https://doi.org/10.1175/2010JCLI3575.1.

——, K. A. Emanuel, and A. H. Sobel, 2007: Use of a genesis potential index to diagnose ENSO effects on tropical cyclone genesis. *J. Climate*, **20**, 4819–4834, https://doi.org/10.1175/JCLI4282.1.

Chelliah, M., and G. D. Bell, 2004: Tropical multidecadal and interannual climate variability in the NCEP–NCAR reanalysis. *J. Climate*, **17**, 1777–1803, https://doi.org/10.1175/1520-0442(2004)017<1777:TMAICV>2.0.CO;2.

Chiang, J., and D. Vimont, 2004: Analogous Pacific and Atlantic meridional modes of tropical atmosphere–ocean variability. *J. Climate*, **17**, 4143–4158, https://doi.org/10.1175/JCLI4953.1.

CPC, 2020: Background information: North Atlantic hurricane season. NOAA Center for Weather and Climate Prediction, accessed 24 February 2021, https://www.cpc.ncep.noaa.gov/products/outlooks/Background.html.

Czaja, A., A. W. Robertson, and T. Huck, 2003: *The Role of Atlantic Ocean–Atmosphere Coupling in Affecting North Atlantic Oscillation Variability*. Amer. Geophys. Union, 147–172, https://doi.org/10.1029/134GM07.

Drouard, M., G. Rivière, and P. Arbogast, 2013: The North Atlantic Oscillation response to large-scale atmospheric anomalies in the northeastern Pacific. *J. Atmos. Sci.*, **70**, 2854–2874, https://doi.org/10.1175/JAS-D-12-0351.1.

——, ——, and ——, 2015: The link between the North Pacific climate variability and the North Atlantic Oscillation via

downstream propagation of synoptic waves. *J. Climate*, **28**, 3957–3976, https://doi.org/10.1175/JCLI-D-14-00552.1.

Franzke, C., S. Lee, and S. B. Feldstein, 2004: Is the North Atlantic Oscillation a breaking wave? *J. Atmos. Sci.*, **61**, 145–160, https://doi.org/10.1175/1520-0469(2004)061<0145:ITNAOA>2.0.CO;2.

Goldenberg, S. B., C. W. Landsea, A. M. Mestas-Nuñez, and W. M. Gray, 2001: The recent increase in Atlantic hurricane activity: Causes and implications. *Science*, **293**, 474–479, https://doi.org/10.1126/science.1060040.

Gray, W. M., 1984: Atlantic seasonal hurricane frequency. Part I: El Niño and 30 mb quasi-biennial oscillation influences. *Mon. Wea. Rev.*, **112**, 1649–1668, https://doi.org/10.1175/1520-0493(1984)112<1649:ASHFPI>2.0.CO;2.

Hersbach, H., and Coauthors, 2020: The ERA5 global reanalysis. *Quart. J. Roy. Meteor. Soc.*, **146**, 1999–2049, https://doi.org/10.1002/qj.3803.

Jones, J. J., M. M. Bell, and P. J. Klotzbach, 2020: Tropical and subtropical North Atlantic vertical wind shear and seasonal tropical cyclone activity. *J. Climate*, **33**, 5413–5426, https://doi.org/10.1175/JCLI-D-19-0474.1.

Klotzbach, P. J., and W. M. Gray, 2004: Updated 6–11-month prediction of Atlantic basin seasonal hurricane activity. *Wea. Forecasting*, **19**, 917–934, https://doi.org/10.1175/1520-0434(2004)019<0917:UMPOAB>2.0.CO;2.

——, and ——, 2008: Multidecadal variability in North Atlantic tropical cyclone activity. *J. Climate*, **21**, 3929–3935, https://doi.org/10.1175/2008JCLI2162.1.

——, and ——, 2013: Summary of 2013 Atlantic tropical cyclone activity and verification of authors' seasonal and two-week forecasts. Accessed 30 July 2020, https://tropical.colostate.edu/Forecast/Archived_Forecasts/2010s/2013-11.pdf.

——, M. A. Saunders, G. D. Bell, and E. S. Blake, 2017: North Atlantic seasonal hurricane prediction: Underlying science and an evaluation of statistical models. *Climate Extremes: Patterns and Mechanisms*, *Geophys. Monogr.*, Vol. 226, Amer. Geophys. Union, 315–328–328, https://doi.org/10.1002/9781119068020.ch19.

——, M. M. Bell, and J. Jones, 2019: Extended range forecast of Atlantic seasonal hurricane activity and landfall strike probability for 2019. Colorado State University, accessed 30 August 2020, https://tropical.colostate.edu/Forecast/Archived_Forecasts/2010s/2019-04.pdf.

——, ——, and ——, 2020: Extended range forecast of Atlantic seasonal hurricane activity and landfall strike probability for 2020. Colorado State University, accessed 30 April 2020, https://tropical.colostate.edu/Forecast/2020-04.pdf.

Kossin, J. P., and D. J. Vimont, 2007: A more general framework for understanding Atlantic hurricane variability and trends. *Bull. Amer. Meteor. Soc.*, **88**, 1767–1782, https://doi.org/10.1175/BAMS-88-11-1767.

Kunz, A., M. Sprenger, and H. Wernli, 2015: Climatology of potential vorticity streamers and associated isentropic transport pathways across PV gradient barriers. *J. Geophys. Res. Atmos.*, **120**, 3802–3821, https://doi.org/10.1002/2014JD022615.

Landsea, C. W., and J. L. Franklin, 2013: Atlantic hurricane database uncertainty and presentation of a new database format. *Mon. Wea. Rev.*, **141**, 3576–3592, https://doi.org/10.1175/MWR-D-12-00254.1.

Li, W., Z. Wang, G. Zhang, M. S. Peng, S. G. Benjamin, and M. Zhao, 2018: Subseasonal variability of Rossby wave breaking and impacts on tropical cyclones during the North Atlantic warm season. *J. Climate*, **31**, 9679–9695, https://doi.org/10.1175/JCLI-D-17-0880.1.

Madden, R. A., and P. R. Julian, 1972: Description of global-scale circulation cells in the tropics with a 40–50 day period. *J. Atmos. Sci.*, **29**, 1109–1123, https://doi.org/10.1175/1520-0469(1972)029<1109:DOGSCC>2.0.CO;2..

Mariotti, A., and Coauthors, 2020: Windows of opportunity for skillful forecasts subseasonal to seasonal and beyond. *Bull. Amer. Meteor. Soc.*, **101**, E608–E625, https://doi.org/10.1175/BAMS-D-18-0326.1.

Martius, O., C. Schwierz, and M. Sprenger, 2008: Dynamical tropopause variability and potential vorticity streamers in the Northern Hemisphere: A climatological analysis. *Adv. Atmos. Sci.*, **25**, 367–380, https://doi.org/10.1007/s00376-008-0367-z.

McIntyre, M. E., and T. Palmer, 1983: Breaking planetary waves in the stratosphere. *Nature*, **305**, 593–600, https://doi.org/10.1038/305593a0.

Ogi, M., Y. Tachibana, and K. Yamazaki, 2003: Impact of the wintertime North Atlantic Oscillation (NAO) on the summertime atmospheric circulation. *Geophys. Res. Lett.*, **30**, 1704, https://doi.org/10.1029/2003GL017280.

Papin, P. P., 2017: Variations in potential vorticity streamer activity: Development pathways, environmental impacts, and links to tropical cyclone activity in the North Atlantic basin. Ph.D. thesis, University at Albany, State University of New York, 225 pp., https://www.proquest.com/openview/bcc1d48dc74c82096977fb1d27956a22/1?pq-origsite=gscholar&cbl=18750&diss=y.

——, L. F. Bosart, and R. D. Torn, 2020: A feature-based approach to classifying summertime potential vorticity streamers linked to Rossby wave breaking in the North Atlantic basin. *J. Climate*, **33**, 5953–5969, https://doi.org/10.1175/JCLI-D-19-0812.1.

Patricola, C. M., R. Saravanan, and P. Chang, 2014: The impact of the El Niño–Southern Oscillation and Atlantic meridional mode on seasonal Atlantic tropical cyclone activity. *J. Climate*, **27**, 5311–5328, https://doi.org/10.1175/JCLI-D-13-00687.1.

Postel, G. A., and M. H. Hitchman, 1999: A climatology of Rossby wave breaking along the subtropical tropopause. *J. Atmos. Sci.*, **56**, 359–373, https://doi.org/10.1175/1520-0469(1999)056<0359:ACORWB>2.0.CO;2.

Reynolds, R. W., N. A. Rayner, T. M. Smith, D. C. Stokes, and W. Wang, 2002: An improved in situ and satellite SST analysis for climate. *J. Climate*, **15**, 1609–1625, https://doi.org/10.1175/1520-0442(2002)015<1609:AIISAS>2.0.CO;2.

Saunders, M. A., P. J. Klotzbach, A. S. R. Lea, C. J. Schreck, and M. M. Bell, 2020: Quantifying the probability and causes of the surprisingly active 2018 North Atlantic hurricane season. *Earth Space Sci.*, **7**, e2019EA000852, https://doi.org/10.1029/2019EA000852.

Scaife, A. A., and Coauthors, 2014: Skillful long-range prediction of European and North American winters. *Geophys. Res. Lett.*, **41**, 2514–2519, https://doi.org/10.1002/2014GL059637.

Trenberth, K., 2020: The Climate Data Guide: Niño SST indices (Niño 1 + 2, 3, 3.4, 4; ONI and TNI). National Center for Atmospheric Research, accessed 23 July 2020, https://climatedataguide.ucar.edu/climate-data/nino-sst-indices-nino-12-3-34-4-oni-and-tni.

von Storch, H. H. and F. W. Zwiers, 1999: *Statistical Analysis in Climate Research*. Cambridge University Press, 484 pp.

Wilks, D. S., 2011: *Statistical Methods in the Atmospheric Sciences*. Academic Press, 676 pp.

WMO, 2017: *WMO Guidelines on the Calculation of Climate Normals*. World Meteorological Organization, WMO-No. 1203, 18 pp., https://library.wmo.int/doc_num.php?explnum_id=4166.

Wood, K. M., P. J. Klotzbach, J. M. Collins, L.-P. Caron, R. E. Truchelut, and C. J. Schreck, 2020: Factors affecting the 2019 Atlantic hurricane season and the role of the Indian Ocean dipole. *Geophys. Res. Lett.*, **47**, e2020GL087781, https://doi.org/10.1029/2020GL087781.

Woollings, T., B. Hoskins, M. Blackburn, and P. Berrisford, 2008: A new Rossby wave-breaking interpretation of the North Atlantic Oscillation. *J. Atmos. Sci.*, **65**, 609–626, https://doi.org/10.1175/2007JAS2347.1.

——, A. Hannachi, and B. Hoskins, 2010: Variability of the North Atlantic eddy-driven jet stream. *Quart. J. Roy. Meteor. Soc.*, **136**, 856–868, https://doi.org/10.1002/qj.625.

Zavadoff, B. L., and B. P. Kirtman, 2019: North Atlantic summertime anticyclonic Rossby wave breaking: Climatology, impacts, and connections to the Pacific decadal oscillation. *J. Climate*, **32**, 485–500, https://doi.org/10.1175/JCLI-D-18-0304.1.

Zhang, G., and Z. Wang, 2019: North Atlantic Rossby wave breaking during the hurricane season: Association with tropical and extratropical variability. *J. Climate*, **32**, 3777–3801, https://doi.org/10.1175/JCLI-D-18-0299.1.

——, ——, T. J. Dunkerton, M. S. Peng, and G. Magnusdottir, 2016: Extratropical impacts on Atlantic tropical cyclone activity. *J. Atmos. Sci.*, **73**, 1401–1418, https://doi.org/10.1175/JAS-D-15-0154.1.

——, ——, M. S. Peng, and G. Magnusdottir, 2017: Characteristics and impacts of extratropical Rossby wave breaking during the Atlantic hurricane season. *J. Climate*, **30**, 2363–2379, https://doi.org/10.1175/JCLI-D-16-0425.1.